Quantification and demonstration of the collective constriction-by-ratchet mechanism in the dynamin molecular motor

Oleg M. Ganichkin[a], Renee Vancraenenbroeck[b,1], Gabriel Rosenblum[b], Hagen Hofmann[b], Alexander S. Mikhailov[c,d], Oliver Daumke[a,e,2], and Jeffrey K. Noel[a,c,2]

[a]Crystallography, Max Delbrück Center for Molecular Medicine in the Helmholtz Association, 13125 Berlin, Germany; [b]Department of Chemical and Structural Biology, Weizmann Institute of Science, 76100 Rehovot, Israel; [c]Department of Physical Chemistry, Fritz Haber Institute of the Max Planck Society, 14195 Berlin, Germany; [d]Computational Molecular Biophysics, Nano Life Science Institute, Kanazawa University, Kanazawa 920-1192, Japan; and [e]Institute for Chemistry and Biochemistry, Free University of Berlin, 14195 Berlin, Germany

Dynamin oligomerizes into helical filaments on tubular membrane templates and, through constriction, cleaves them in a GTPase-driven way. Structural observations of GTP-dependent cross-bridges between neighboring filament turns have led to the suggestion that dynamin operates as a molecular ratchet motor. However, the proof of such mechanism remains absent. Particularly, it is not known whether a powerful enough stroke is produced and how the motor modules would cooperate in the constriction process. Here, we characterized the dynamin motor modules by single-molecule Förster resonance energy transfer (smFRET) and found strong nucleotide-dependent conformational preferences. Integrating smFRET with molecular dynamics simulations allowed us to estimate the forces generated in a power stroke. Subsequently, the quantitative force data and the measured kinetics of the GTPase cycle were incorporated into a model including both a dynamin filament, with explicit motor cross-bridges, and a realistic deformable membrane template. In our simulations, collective constriction of the membrane by dynamin motor modules, based on the ratchet mechanism, is directly reproduced and analyzed. Functional parallels between the dynamin system and actomyosin in the muscle are seen. Through concerted action of the motors, tight membrane constriction to the hemifission radius can be reached. Our experimental and computational study provides an example of how collective motor action in megadalton molecular assemblies can be approached and explicitly resolved.

endocytosis | biomembranes | elastic filament | Canham–Helfrich | torque

Dynamin is a mechanochemical GTPase that plays a central role in clathrin-mediated endocytosis (CME) (1–4). The 100-kDa protein polymerizes into helical filaments that coil around the necks of vesicles budding from the membrane. In the presence of guanosine-5'-triphosphate (GTP), such filaments constrict, whereas GTP hydrolysis is necessary to cut the neck, thus allowing the vesicle to separate. This process is crucial for cellular nutrient uptake and for synaptic transmission. Mutations in dynamin are associated with severe neurodegenerative disease and muscular disorders (5). Structural studies have detailed the dynamin filament structure on membrane tubes and observed the filament's ability to form nucleotide-dependent cross-bridges between its neighboring turns (6, 7). These studies, in tandem with biophysical experiments showing GTPase-driven torque generation by dynamin filaments (8–10), have led to proposals that dynamin functions as a molecular ratchet motor (11–13). Confirming this hypothesis requires a molecular-level understanding of the principal GTP-dependent motor function and showing that the candidate power stroke (6) can provide sufficient force to drive membrane constriction. So far, theoretical studies of dynamin have concentrated on the elastic properties of dynamin filaments (14–16) and on the effects exhibited by passive elastic filaments on the membranes (17, 18). The nonequilibrium motor activity of dynamin, based on GTP hydrolysis, was treated only in a phenomenological way (9, 19).

Dynamin consists of five domains (Fig. 1A) (20, 21). Its stalks polymerize into a helical filament whose elementary units are criss-cross stalk dimers. The filament is anchored to the membrane by pleckstrin homology (PH) domains connected by flexible linkers to the stalk. GTPase (G) domains are connected to the filament via bundle signaling elements (BSEs). The disordered C-terminal proline-rich domain (PRD) is involved in recruitment to membrane necks. Hinge 1 and hinge 2 form flexible joints between BSEs and the stalk and between the G domain and BSEs, respectively. We refer to the combination of the G domain and BSE as the motor module (MM) of dynamin (Fig. 1A) (6, 22, 23).

When dynamin is assembled into a helical filament, G domains in adjacent rungs are optimally oriented for cross-dimerization (7), which can explain the enhancement of GTPase activity in the presence of membranes (23). Moreover, the conformation of dynamin's MM is sensitive to its nucleotide state. In the presence

---
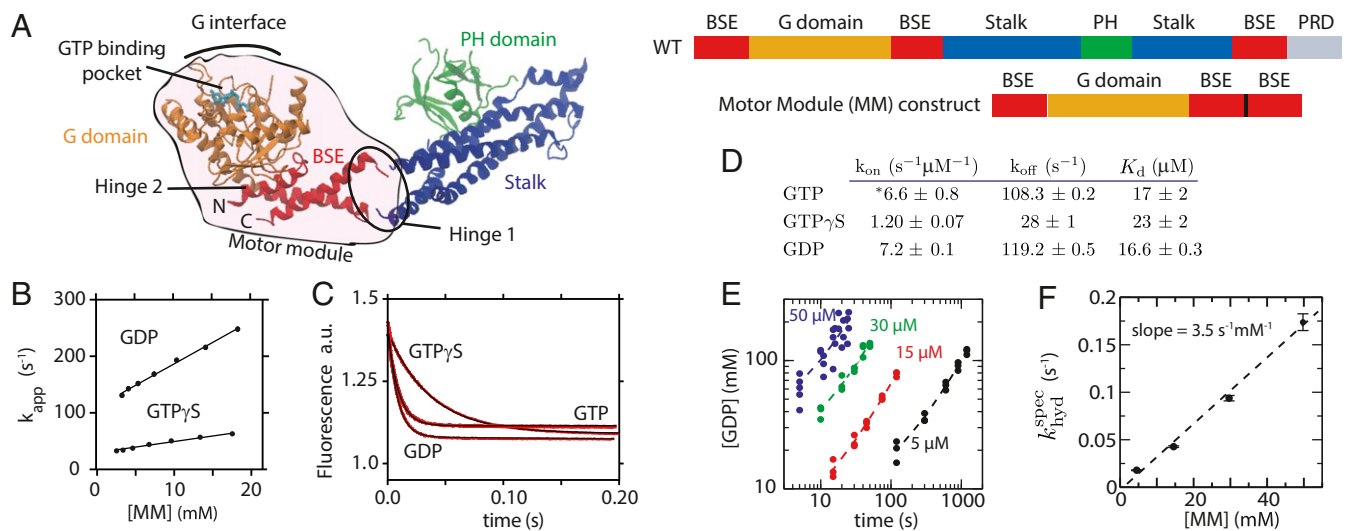
BIOPHYSICS AND COMPUTATIONAL BIOLOGY

Fig. 1. Kinetic characterization of the dynamin motor module. (*A*) The dynamin monomer has four structurally characterized domains (Protein Data Bank 3SNH) (20). The motor module (MM) contains the G domain and the BSE. A continuous MM construct was created by fusing the third helix of the BSE onto the N-terminal portion of the dynamin sequence. (*B*) Association rate constants are obtained from the slope of k_{app} versus MM concentration. See *SI Appendix*, Fig. S1 for mant-GTP association curves. (*C*) Mant-nucleotide dissociation rates were measured in stopped-flow experiments by mixing with excess unlabeled nucleotide. (*D*) Table of determined mant-nucleotide binding/dissociation rates of the MM construct. K_d is defined by the ratio k_{off}/k_{on}. *GTP on rate value is determined from kinetic modeling of GTPase activity (*SI Appendix*, section S1.A.2) because mant binding did not show a single exponential fluorescence increase for mant-GTP (*SI Appendix*, Fig. S1). (*E*) GDP production as a function of time in the linear regime for increasing concentrations of MM and an initial GTP concentration of 1 mM. Dashed lines are linear fits to three independent experiments. (*F*) Slope from *E* divided by the protein concentration gives the specific hydrolysis rate (k_{hyd}^{spec}). Linear dependence of the specific hydrolysis rate on protein concentration indicates that GTPase activity is controlled by dimerization (*SI Appendix*, section S1.A.1).

of the nonhydrolyzable GTP analog β, γ-methyleneguanosine 5′-triphosphate (GMPPCP), the MM crystallized in an open BSE conformation (6), whereas a closed conformation of the BSE was observed in the nucleotide-free state or when bound to guanosine-5′-diphosphate (GDP) or to GDP·AlF$_4^-$, a mimic of the transition state of GTP hydrolysis (20, 21, 23, 24). While this structural shift is the obvious candidate for the power stroke driving motor function, it remains unknown how strong it is, since even small energy preferences might result in the different structural states captured in the available structures. For example, in crystallographic studies, a dynamin family member, MxA, shows open and closed states in the GMPPCP- and GDP-bound states, respectively (25), but only weak nucleotide-dependent preferences in solution (26).

In this study, kinetic measurements for the GTPase cycle of the dynamin MM are first performed. After that, we explore nucleotide-dependent conformational changes in the MM using single-molecule FRET experiments. Their results, in conjunction with molecular modeling, are then used to quantify the forces generated by single dynamin motors and to refine the ratchet effect. Next, we incorporate the determined forces and the measured kinetics into a polymer-like computational model that resolves individual dynamin motors and includes a deformable membrane template with lipid flows within it. Direct simulations of the model reproduce collective tight constriction of membrane necks down to the hemifission radius by dynamin filaments in the presence of GTP.

Results

To study the kinetic and energetic parameters of a single dynamin motor, we have worked with a MM construct containing only the G domain and BSE (23) (Fig. 1*A*). This allows clean interpretation of nucleotide on and off rates, as it removes the complicating process of tetramers (or higher oligomers) associating via their G interfaces. While clarity in this respect could also be achieved with a full-length, but nonoligomerizing mutant, a full-length

monomer may enable G-domain interactions with the stalk or PH domain that are disallowed in the membrane-bound filament. Therefore, using the MM construct for the single-molecule FRET (smFRET) experiments allows us to ensure we are capturing the intrinsic G-domain/BSE conformational ensemble.

Exploring Dynamin's GTPase Cycle. Nucleotide binding and dissociation rates to this construct were evaluated using stopped-flow experiments with fluorescently labeled $2′(3′)$-O-(N-methylanthraniloyl) (mant)-nucleotides (Fig. 1 *B* and *C* and *SI Appendix*, Fig. S1*A*). The affinities for GTP and GDP were both in the low micromolar range (Fig. 1*D*). Therefore, at physiological nucleotide concentrations of GTP (300 μM) and GDP (30 μM) (27), about 90% of monomeric MMs in the cell are bound to GTP. Previous measurements (28, 29) reporting even higher GTP affinity were performed using full-length dynamin, thus also including possible contributions from nucleotide-induced assembly that enhance nucleotide occupancy.

A low basal rate of GTPase hydrolysis and a linear dependence of the specific hydrolysis rate k_{hyd}^{spec} on MM concentration were observed (Fig. 1 *E* and *F* and *SI Appendix*, section S1.A.1), confirming that MM dimerization should precede the hydrolysis and is required for it. These GTPase measurements additionally indicated that the GTP-bound dimer has a weak affinity ($K_d^{dimer} \gg 50$ μM).

Running the GTPase assay beyond the linear regime allows GDP to compete with GTP for the active site. Therefore, the GTPase kinetics of such an experiment contain information on the relative affinity between GTP and GDP for the MM. A kinetic model was devised to fit experimental traces and determine unknown parameters (*SI Appendix*, section S1.A.2). Varying this setup with different initial conditions (*SI Appendix*, Fig. S1 *B* and *D*) allowed us to estimate an apparent GTP on rate of 6.6 s^{-1}·μM^{-1}, which was not straightforward to determine with mant-GTP (*SI Appendix*, Fig. S1*A*).

Measuring nucleotide exchange kinetics within the dimer is complicated by the low MM dimerization affinity. To resolve this difficulty, we engineered a Zn^{2+}-dependent metal bridge by introducing histidines into the G interface (MM-HH). X-ray crystallography confirmed that Zn^{2+} stabilized a similar dimer arrangement as previously observed in the GDP-bound MM dimer (24) (*SI Appendix*, Fig. S2 and Table S1). In line with our predictions, addition of Zn^{2+} to this double histidine (MM-HH) construct induced dimerization in gel-filtration (*SI Appendix*, Fig. S3*A*) and FRET experiments (*SI Appendix*, Fig. S3*B*). Of note, addition of GTPγS reduced mutant dimer formation (*SI Appendix*, Fig. S3*B*).

Dimer dissociation rates were measured by FRET experiments and stopped-flow. Addition of GDP slowed the dimer dissociation rate of the Zn^{2+}-stabilized MM-HH dimer sixfold relative to the apo state (*SI Appendix*, Fig. S3 *D* and *E*), consistent with a long-lived posthydrolysis dimeric state. Addition of GTP greatly accelerated dimer dissociation, suggesting that the GTP-bound state is not compatible with the engineered Zn^{2+} bridge. Relevant to the motor cycle, mant-GDP did not bind to empty Zn^{2+}-stabilized MM-HH dimers. Furthermore, mant-GDP dissociation from MM-HH dimers was 100-fold slower in the presence of Zn^{2+} (*SI Appendix*, Fig. S3 *G–J*). These observations imply that nucleotide exchange is greatly reduced in the MM dimer, therefore simplifying dynamin's motor cycle (see below).

Nucleotide-Dependent Motor Module Conformation in Solution. To characterize nucleotide-dependent conformational changes in the MM, single-molecule FRET (smFRET) was employed. We monitored the relative orientation of the G domain and BSE by introducing a pair of FRET dyes, one in BSE and the other in the G domain (Fig. 2 *A* and *B* and *SI Appendix*, Fig. S4). The experiments were performed on freely diffusing MMs.

In the presence of GTP, three populations could be discerned (Fig. 2*A* and *SI Appendix*, Fig. S4*C*) by fitting to Gaussian distributions: a dominant open state with a FRET efficiency peak

(E) at $E = 0.18$, an intermediate state at $E = 0.39$, and a closed state at $E = 0.77$. The peak values of the open and closed states were in excellent agreement with the predicted mean FRET efficiencies from simulations based on the crystal structures of 0.19 and 0.79, respectively (Fig. 2*C*). The GTP analogs (GMPPCP and GTPγS) showed bimodal distributions. Interestingly, the low FRET peak for GTPγS coincided with the intermediate peak found in the presence of GTP. Note that the nonhydrolyzable GTP analogs produce different structural ensembles from those found with GTP. Care has therefore to be taken when interpreting experiments using GTP analogs. Remarkably, in absence of nucleotides or in presence of GDP, the conformational distributions were strongly shifted toward the closed state. For the apo protein, the position of the FRET peak coincided with that of the GTP-bound closed state. For GDP, the closed state was shifted slightly higher to $E = 0.8$, consistent with crystal data (*SI Appendix*, Fig. S4*D*).

Ensemble stopped-flow measurements were used to obtain relaxation rates to the equilibrium distributions. The rate of opening, i.e., of a transition from apo (closed) to the GTP-bound state, was fitted to a single exponential with a time constant of approximately $300\ s^{-1}$ (Fig. 2 *D* and *E*). This rate contains both nucleotide binding and the conformational change. However, since nucleotide binding at 1 mM GTP is much faster than opening, the measured rate must correspond to the conformational change. Because $300\ s^{-1}$ is large compared to the overall turnover rate of the GTPase cycle, GTP binding and opening are combined in our summary of the GTPase cycle (Fig. 3). The rate of closing in solution, induced by GTP dissociation, is larger than $105\ s^{-1}$ (*SI Appendix*, Fig. S4*E*). However, this parameter is of little relevance for dynamin's function since, in the filament, closing takes place within a dimer and under load.

Operation Cycle of the Dynamin Motor. The kinetic and conformational results are summarized in the diagram of the GTPase cycle (Fig. 3). The GTP-bound MM monomers are predominantly
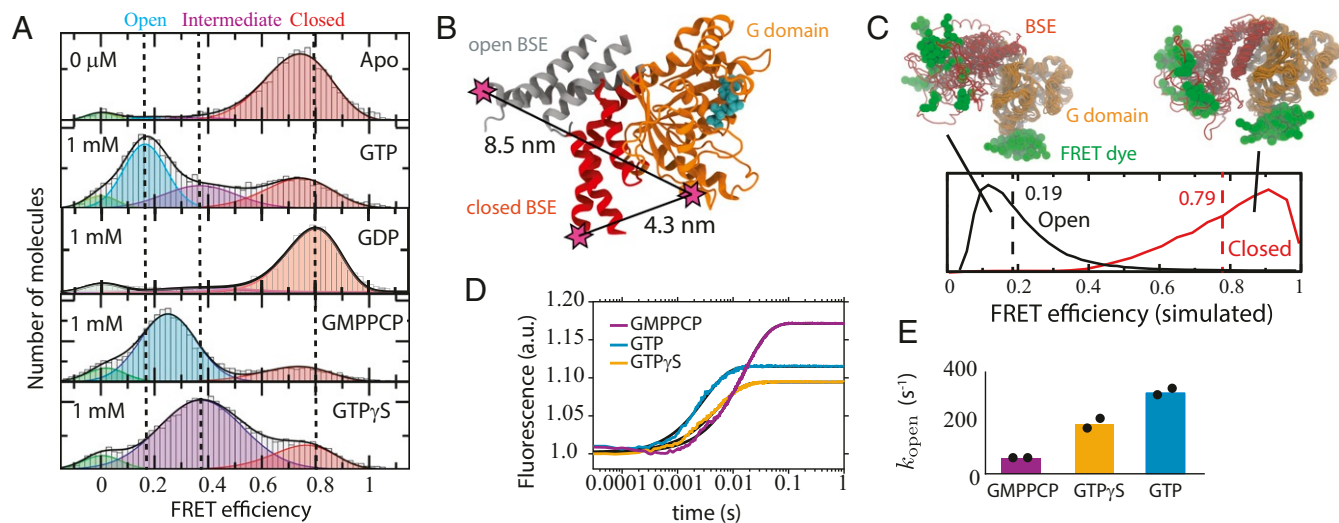

Fig. 2. FRET measurements reveal the dependence of the G domain/BSE conformation on nucleotide state. (*A*) smFRET histograms were fitted to a four–Gaussian-state model and were colored according to the approximate position of the peaks: red, closed; purple, intermediate open; cyan, open; green, molecules lacking an active acceptor dye. Apo and GDP states peak at high FRET while the other ligands show heterogeneity. The picomolar concentrations of MM used for smFRET ensured that the ensembles corresponded to MM monomers. (*B*) Distance between FRET labeling sites based on the crystallographic open (GMPPCP-bound) (6) and closed (GDP-bound) (24) BSE orientations. Cyan spheres show the nucleotide-binding location. (*C*) Dashed lines (solid lines) show the average FRET (FRET distribution) from molecular simulations based on the open or closed crystal structures. The close correspondence of the average FRET with the smFRET data provides evidence that the crystal structures describe the high and low FRET states seen in smFRET. Several snapshots from the two simulation ensembles are displayed with their G domains aligned and FRET dye represented as green spheres. (*D*) Kinetics of opening were measured by mixing apo, doubly labeled MM with saturating concentrations (1 mM) of nucleotide. Single exponential fits to donor fluorescence are shown. (*E*) The opening rate determined by averaging the single exponential rate constants from two independent experiments (shown as black dots). The measured rate involves two processes: nucleotide binding and the conformational change.
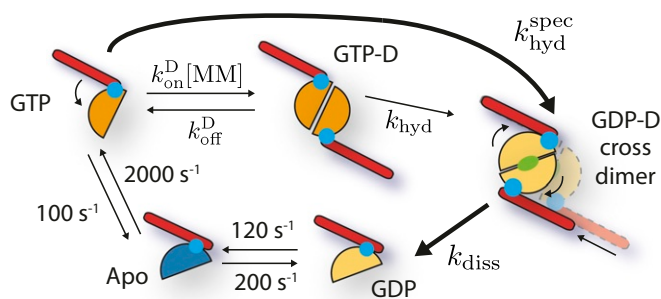
Ganichkin et al.
Quantification and demonstration of the collective constriction-by-ratchet mechanism in the dynamin molecular motor

PNAS | 3 of 11
https://doi.org/10.1073/pnas.2101144118

Fig. 3. GTPase cycle for the MM. Ligand binding kinetics are taken from Fig. 1 assuming physiological concentrations of 300 μM GTP and 30 μM GDP. [MM] refers to the concentration of GTP-bound MM. The green dot indicates the presence of inorganic phosphate. Experimental measurements of GTPase activity in the presence of membranes set a lower limit of 4 s^{-1} (20) for the whole cycle.

open and must dimerize (GTP-D) to enable hydrolysis. Hydrolysis leads to a strong preference in the MM dimer (GDP-D) for the closed state. Using the MM-HH mutant, we confirmed that the GDP-bound dimer is strongly closed in a similar fashion to the GDP-bound monomer (*SI Appendix*, Fig. S3C). The MM dimer in its GDP·inorganic phosphate (Pi) or GDP-bound states dissociates only slowly, consistent with the high stability of the dimers bound to GDP·AlF$_4^-$ (23) and with our kinetic results with GDP (*SI Appendix*, Fig. S3E). Nucleotide exchange within the MM dimer is slow and can therefore be neglected in the scheme (*SI Appendix*, Fig. S3 *I and J*). Once monomeric, GDP exchanges in favor of GTP, thus completing the cycle.

Note that hydrolysis (k_{hyd}) and posthydrolysis MM dimer dissociation (k_{diss}) rates, as well as the dimerization (k_{on}^D) and

dissociation (k_{off}^D) rates of MM monomers in the GTP-bound state, remain yet unknown, meaning the entire GTPase cycle could not be precisely specified. Therefore, in our model simulations, various values of the effective hydrolysis rate k_{hyd}^{spec} and of k_{diss} were chosen and explored (see *SI Appendix*, section S1.B for details). Measurements of GTPase activity in the presence of membranes set a lower limit of 4 s^{-1} (20) for its turnover rate. The slowest measured rate in the forward direction is that of GDP dissociation at 120 s^{-1}, yielding an upper limit for the overall turnover rate.

Determination of Generated Forces. In the helical filament, a pair of GTP-bound MMs belonging to adjacent rungs can dimerize to form a cross-bridge (Fig. 4A). Upon hydrolysis in both MMs, the equilibrium conformation of the dimer shifts from the open to the closed ensemble, thus shortening its equilibrium bridging length and creating a contracting force along it.

The length of a bridging MM dimer is quantified by the end-to-end length distributions $P_{GTP}(\ell)$ and $P_{GDP}(\ell)$. Although distance distributions can be yielded by smFRET, our FRET experiments are limited to MM monomers. Therefore, probability distributions over ℓ for the two nucleotide states were obtained from MD simulations of a dual-basin structure-based model (31) (see *SI Appendix*, Fig. S5 and section S1.C for a detailed discussion). The MM dimer representation was built by connecting two MM monomers, each described by the dual-basin model, at their G interface (Fig. 4B). Importantly, the simulations incorporated the experimentally observed energetics by enforcing that the simulated FRET distribution in each MM monomer match the observed smFRET distribution of open and closed states (*SI Appendix*, Fig. S5).

The free energy profile of a GTP-bound MM dimer along ℓ shows a single broad basin (Fig. 4C). This implies that initial cross-bridges can form over a wide range of distances.
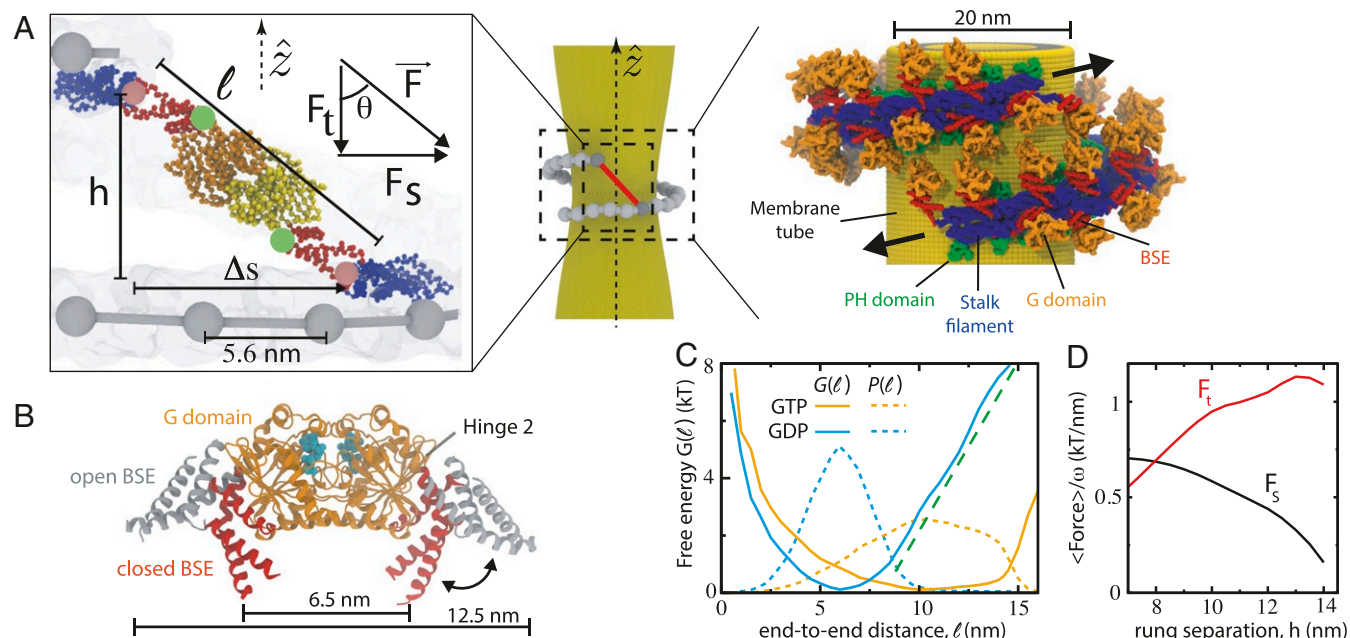
Fig. 4. Determination of forces. (*A*) (*Center*) An MM dimer forms a cross-bridge (red) between two neighboring filament rungs. (*Left*) Definition of cross-bridge geometry. The length ℓ is defined as the distance between hinge 1 connections (pink circles); green circles indicate hinges 2. (*Right*) A cartoon representation based on the cryo-electron microscopy structure of the "nonconstricted" filament (30) shows the overall architecture of the dynamin filament. (*B*) Overlay of open and closed G-domain dimer crystal structures. Estimates for ℓ, i.e., the distance between hinge 1 attachment points, are shown. Cyan spheres show the nucleotide-binding location. (*C*) Free energies $G_{GTP}(\ell)$ (orange) and $G_{GDP}(\ell)$ (blue) obtained by MD simulations for MM dimers. The respective distributions $P_{GTP}(\ell)$ and $P_{GDP}(\ell)$ of distances are shown by orange and blue dashed lines. The dashed green line has a slope of $F_0 = 1.3$ k$_B$T/nm (5.2 pN). (*D*) Mean stall forces along the filament (black) and in the transverse direction (red) as functions of the separation h between the rungs (see *SI Appendix* for details).

This property is enabled by the heterogeneity of the GTP-bound conformations (Fig. 2A). In contrast, the free energy G_{GDP} for GDP-bound MM dimers has a single narrow minimum at a shorter ℓ (Fig. 4C). The effective contracting force along ℓ is given by $F(\ell) = -dG_{GDP}(\ell)/d\ell$. In the simulations of membrane constriction, this instantaneous force, produced by a MM dimer when it is in the GDP-bound state and has length ℓ, is employed. Remarkably, the force remains approximately constant (Fig. 4C) at $F_0 = 1.3$ k_BT/nm over the range of ℓ from 8 to 14 nm.

To transform the cyclic changes of the GTPase cycle (Fig. 3) into a directed force acting on the helical filament, a ratchet mechanism must be employed. The principal feature of the ratchet is a differential response to the power stroke and the recovery stroke. The transition from an open to a closed conformation, representing a power stroke, takes place when the two MMs from the neighboring rungs are dimerized and forming a cross-bridge. The recovery stroke, corresponding to the reverse transition to the open state, however, occurs only in the monomeric MM state, i.e., when the bridge is absent. Therefore, force is applied to the filament only in one part of the GTPase cycle.

There is, however, an additional component to the ratchet effect. If it were equally probable that the cross-bridges slanted to the right and to the left, shortening of such links could not generate a net force. Hence, a directional bias in slanting is needed. For dynamin's right-handed helix, preferentially slanting the upper MM to the right and the lower MM to the left with respect to the stalk filament would generate a constricting torque (i.e., as in Fig. 4A). Indeed, the comparison of all available dynamin structures has shown that hinge 1 is biased in this way, and our molecular dynamics (MD) simulations have indicated that the biased orientation is robust to thermal fluctuations (*SI Appendix*, Fig. S6).

One can calculate the mean force generated by a pair of MMs over many GTPase cycles by averaging the force applied between two immobilized stalk filaments (under stall conditions). Note that time averaging is equivalent to statistical averaging over an ensemble. Using the distributions for ℓ from MD simulations and the geometry of Fig. 4C, the component of the mean force acting along the filament is $\langle F_s \rangle = \omega \int_{\ell_{min}}^{\ell_{max}} P_{GTP}(\ell) F(\ell) \sin \theta(\ell) d\ell$, where θ is the slant angle and ω is the probability (often referred to as the duty ratio) (32) to find a MM in the dimerized state. Because of the ratchet property of hinge 1, only configurations with positive displacements Δs are included into the average. The transverse component $\langle F_t \rangle$ is given by the same equation with $\sin \theta$ replaced by $-\cos \theta$.

The mean forces $\langle F_s \rangle$ and $\langle F_t \rangle$ are shown as functions of the rung separation h in Fig. 4D. Note that the derived estimates are sensitive to the relative weights of the open and closed conformations in a GDP-bound MM (*SI Appendix*, Fig. S5 *C and D*). Since the observed frequency of the open conformation in smFRET is likely enhanced by experimental noise, they should be viewed as providing the lower bounds for the force.

The torque, locally applied to the filament by a MM dimer motor, is $\langle F_s \rangle R$, where R is the filament radius. Assuming that a MM is found predominantly in the dimerized state, i.e., ω is near unity, $\langle F_s \rangle$ is 2.9 pN (0.7 k_BT/nm) and the mean torque generated by a single motor in the nonconstricted state (with $h = 8$ nm and $R = 25$ nm as in Fig. 4A) is 72 pN·nm. When many MMs are simultaneously cooperating, large torques on the order of 1 nN·nm can be produced, similar in size to what has been experimentally observed (10). These collective effects are discussed in the next section.

Collective Operation of Motor Modules and Constriction of Membranes. The MM dimers, connecting neighboring rungs, produce forces that tend to rotate them with respect to one another.

Collectively, they generate the torque applied to the filament. We directly demonstrate this via computer simulations of a mesoscopic model. It was obtained by augmenting the recently developed coarse-grained description of a dynamin polymer filament on a deformable membrane tube (16) to additionally account for the GTPase motor activity of dynamin. In the model, MM dimers are introduced as elastic cross-bridges that connect the polymer beads and apply forces between them. Since each bead corresponds to a dynamin stalk dimer, it has two MMs associated with it. The nucleotide state of each MM is tracked and the GTPase cycle is implemented within it. Dimerization, i.e., formation of a cross-bridge, can occur if both MMs are GTP bound. After the hydrolysis-induced conformational change, the cross-bridge becomes strained and produces, as outlined above, a contracting force $F(\ell)$ for a cross-bridge of instantaneous length ℓ. The MM dimers dissociate (and thus cross-bridges disappear) at rate k_{diss}. See *Materials and Methods* and *SI Appendix*, Fig. S7 for the details.

In endocytosis, constriction and cleavage of membrane necks are performed by short dynamin filaments with only a few tens of MMs (33, 34). Filaments with 28 or 40 beads were therefore probed in our simulations. They were carried out for various MM dimer dissociation rates k_{diss} (Movie S1), thus yielding the regimes with different duty ratios ω (*SI Appendix*, Eq. S8). Fig. 5A gives example snapshots of the initial and final states. The dependence of the final steady-state inner lumen radius (ILR) of the membrane tube on the duty ratio is displayed in Fig. 5B. Tight constriction from 10.5 to 2 to 3 nm ILR is found above $\omega = 0.65$. Increasing the filament length from 28 to 40 significantly decreases the ILR; however, increasing the length beyond 40 beads does not lead to further decreases in ILR.

Imaging of single endocytic pits during CME suggests that dynamin is active from a few seconds to tens of seconds before scission occurs (33, 34). Consistent with this, simulations showed that ILR below 3 nm could be reached within about 1 s for the duty ratios of 0.6 to 0.7 and within 15 s for $\omega = 0.94$ (Fig. 5C). Examination revealed that constriction speed was limited by k_{diss}. When MM dimer dissociation is slow (corresponding to large duty ratios), cross-bridges continue to stay after the power stroke and are driven along with the sliding filament to reverse their slants (Fig. 5D). The misoriented cross-bridges get oppositely stretched and block the constriction.

In the actomyosin system, key kinetic steps are sensitive to strain (35–38) and similar sensitivity may be present in dynamin. In our model, strain control could be implemented by introducing immediate dissociation of MM dimers once their slant is reversed and they become stretched. For a 40-bead filament and $\omega = 0.94$, this reduced the time of constriction to 3 nm from 15 s down to 300 ms (Fig. 5C and Movie S2). This effect could underlie the reported fast endocytosis within hundreds of milliseconds (39). Note that strain control affects only the kinetics, since the standing filament in the steady state cannot drive cross-bridges to alter their slants (and therefore the same ILR dependence as in Fig. 5B holds).

In in vitro experiments, scission of membrane tubes by long dynamin filaments can be observed. Surprisingly, such experiments find that breaking of the tube takes place not in the middle of the dynamin coat, but rather at its flanks (10, 40). In line with this finding, our simulations show that constriction by a long filament begins near its ends (Fig. 6 *A and B* and Movie S3) and only later propagates toward the middle. Fission may thus occur at a flank before the steady state has been reached. A simple explanation is that, in the middle of a long filament, a rung is pulled in opposite directions by its two neighboring rungs (Fig. 6 *C and D*). Such cancellation is absent for the terminal turns and, thus, only the motors on the flanks of a long helical filament apply a net torque and contribute to constriction of the membrane. Hence, the work produced by a long dynamin
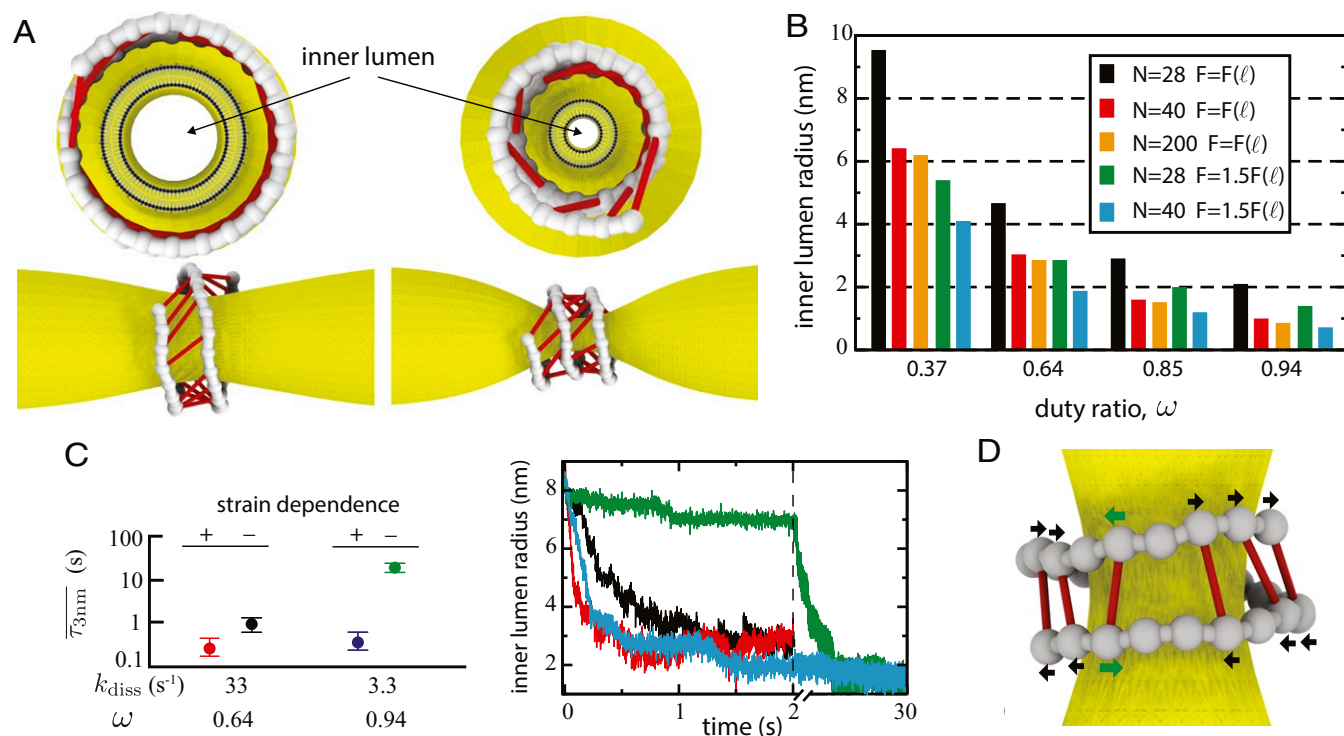
Ganichkin et al.
Quantification and demonstration of the collective constriction-by-ratchet mechanism in the dynamin molecular motor

PNAS | 5 of 11
https://doi.org/10.1073/pnas.2101144118

Fig. 5. Membrane constriction by the dynamin oligomer. (*A*) Snapshots of the initial (*Left*) and final (*Right*) steady states for a filament with $N = 40$ dimers and duty ratio $\omega = 0.75$. Cross-bridges are indicated as red links. The tube is constricted from ILR of 10.5 to 2.5 nm. (*B*) Dependence of the steady-state ILR on the duty ratio ω for different filament lengths N and motor strengths $F(\ell)$. Since the force depends on the population ratio of open and closed FRET states in the GDP-bound ensemble, which can be affected by experimental noise, it may well be larger than in Fig. 4C. The membrane has stiffness of 24 $k_B T$ (6×10^{-20} J) and tension of 0.03 $k_B T/nm^2$. All simulations start from thermal equilibrium in absence of GTP. (*C*) Constriction is much accelerated under a strain-dependent MM dimer dissociation rate (green and black, strain-independent k_{diss}; blue and red, strain-dependent k_{diss}). (*Left*) Average times $\overline{\tau_{3\,nm}}$ to reach an ILR of 3 nm. Horizontal bars indicate the upper and lower quartiles over 50 constriction simulations. (*Right*) Examples of time dependence of the ILR (the same color code as in *Left*). (*D*) Example of a configuration including a blocking link (with green arrows). Bridging GDP-bound MM dimers are shown as red links.

filament becomes independent of its length. Note that, in the employed model, dynamin-coated membrane tubes are assumed to be straight. Therefore, the effects of supercoiling, reported for very long tubes (8, 9), could not be considered here.

Discussion

Since its discovery in the early 1990s (41, 42), dynamin has become the paradigm for studying GTPase-driven membrane remodeling. Biophysical experiments and structural studies have revealed dynamin to be a helical-shaped, torque-producing motor. In the current study, we provide the quantitative basis for the proposed ratchet operation and describe in detail the molecular mechanism whereby dynamin's motor modules collectively induce filament sliding. Our smFRET experiments showed strong nucleotide-dependent shifts, which, in conjunction with molecular modeling, allowed us to estimate the force generated by a single cross-bridge. Then, by incorporating these interactions into an energetically realistic filament-on-a-membrane model, we directly demonstrate that through cooperative action, dynamin's cross-bridges generate sufficient torque to drive strong constriction of biomembrane tubes. Importantly, the principal experimental features of membrane constriction by dynamin are either reproduced in our study or consistent with its results. Dynamin's ability to create torque over a dynamin helix (9) is shown to arise from repeated cycles of interaction between neighboring MMs. It is confirmed that short dynamin helices with 1.5 to 2 turns are sufficient to produce tight constriction (33, 34) and the torque production in the model is consistent with the levels measured experimentally (10). The

fission at the edge of a dynamin coat, observed in the experiments with fluorescent membrane tubes pulled from giant unilamellar vesicles (10) or for nanotubes imaged by high-speed atomic force microscopy (40, 43), can be explained by us. Typical durations of dynamin scission events (33, 39) are in agreement with the theoretic predictions.

The force generated by a single cross-bridge is much less than the overall force the dynamin filament has been experimentally measured to produce (10) and less than the force that is theoretically required for strongly constricting the membrane tube (*SI Appendix*, Fig. S7E). Therefore, strong constriction requires that, at any time, most of the possible cross-bridges are formed (i.e., a high duty ratio) to cooperatively generate a large torque. Note that this cooperation does not come from synchronizing GTPase activity between MMs. Importantly, our simulations have shown that relative sliding of neighboring turns is possible even when MMs are working asynchronously and with large duty ratios. Sliding can be expedited with a strain-dependent dissociation rate.

We noted that nucleotide-dependent conformational changes are much more pronounced in dynamin than in the related MxA protein (26). Whereas for MxA, the ratio of populations of the open to closed states in the presence of GDP was 0.43 (i.e., 30 to 70%), the GDP-bound open state was practically undetectable for dynamin (i.e., a ratio <0.05). Thus, the resulting forces generated are at least three times stronger for dynamin. This highlights the functional difference of dynamin with MxA: MxA works as an antiviral machine that most likely acts on viral nucleocapsids rather than in the remodeling of membranes (44). We therefore
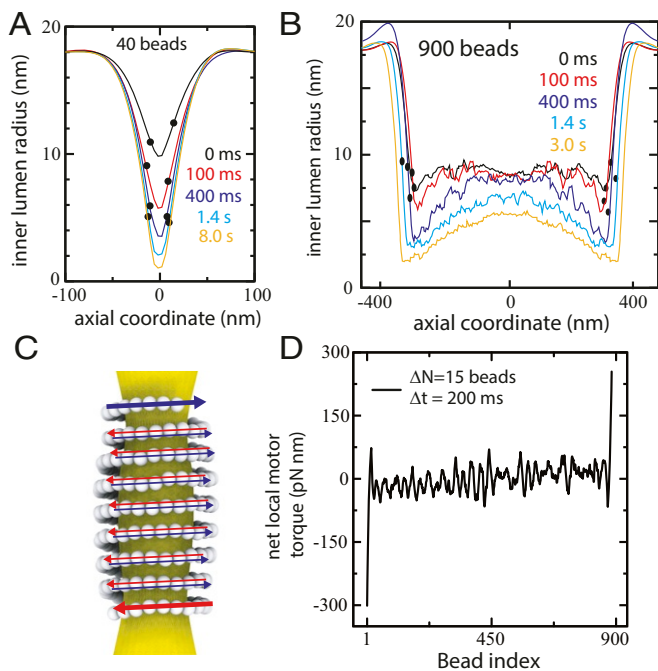
Fig. 6. Long filaments first constrict near their ends. (*A* and *B*) Evolutions of ILR profile under strain control for short ($N = 40$) and long ($N = 900$) filaments. Circles mark the positions of terminal beads. The membrane has stiffness of 24 k_BT (6×10^{-20} J), tension of 0.03 k_BT/nm^2, and $\omega = 0.94$. (*C*) Motor forces in a dynamin coat tend to cancel each other, except for the flanks. Shown is an $N = 200$ filament and cross-bridges are not shown. (*D*) Net motor torque along the helical filament axis, summed over 15 consecutive beads (approximately corresponding to one rung). The bead index specifies the position starting from which the summation is performed. The plotted data are additionally averaged over 200 ms (from 600 to 800 ms in *B*). The net torque almost vanishes everywhere, except the flanks.

expect that the functions of dynamin superfamily members are modulated by tuning the nucleotide-dependent conformational preferences of the MM.

In our simulations, the stalk filament is treated as an elastic ribbon whose local orientation with respect to the membrane remains fixed. The elastic description, developed in ref. 16 and used in the present study, accounts for subtle changes within the tetramer interfaces 1 and 3 that allow the filament to adapt to curvature variations. The interface 2, defining the dynamin dimer, is taken as rigid in our simulations, as supported by the growing number of stalk structures that show a nonchanging stalk interface (7, 20, 44–46). It is also assumed that nucleotide-driven conformational changes are limited to the MM. It should be noted that the proposed PH-domain–coupled tilt deformations of the dynamin filament (47) or filament clustering induced by the transition state analog vanadate (40) could induce deformations in the stalk tetramer that are inconsistent with its soft normal modes (16). These deformations could lead to breakages along the filament, which would provide additional filament ends where torque production and membrane scission could occur.

The membrane is treated in the elastic Helfrich approximation, and lipid flows within it are conserved. Moreover, axial symmetry of the membrane is assumed. The filament sits on the membrane, but is free to slide over it, subject to viscous friction. To account for membrane breakup, a more detailed, molecular-level description for lipid bilayers would have been needed (such as in refs. 18 and 48). Generally, the instability of a membrane tube and hemifission is expected when an ILR below 2 nm is reached (17). Fission can be, however, facilitated by buckling of

the tube (49). It can also be promoted by membrane-bound PH domains whose conformations change within the GTPase cycle (7, 18, 50, 51). The combination of such effects would probably enable membrane breakup even at ILRs of 2 to 3 nm.

As has been previously suggested (2, 12), we find that collective motor activity within the dynamin "nanomuscle" resembles that of actomyosin in the muscle (Fig. 7). In the muscle, a thick myosin filament slides over a thin filament of actin (32). Myosin heads bind to actin so that cross-bridges connecting both filaments are formed. As proposed by H. E. Huxley (52), muscle contraction is effectively due to a combination of cyclic conformational changes and a ratchet effect. Depending on its nucleotide state, myosin alternates between open and closed conformations. The transition from the open to the closed states takes place when the bridge exists; it leads to shortening of the bridge and generation of a pulling force. The reverse transition, however, occurs when the cross-bridge is absent and, therefore, the ratchet is lifted and no force is produced. The muscle is a large assembly where thousands of motors over many filaments operate in parallel.

For dynamin, in the presence of GTP, cross-bridges between adjacent rungs of a helical stalk filament of dynamin are formed through dimerization of neighboring MMs and preferentially in an open state. A posthydrolysis shift to the closed state generates a force pulling the filaments with respect to one another, and hence a torque is produced. Binding of GTP and return to the open state can occur only after the disappearance of the cross-bridge. Remarkably, only tens of motor modules are typically involved in this nanomuscle.

The posthydrolysis dimer dissociation rate k_{diss} plays an important role in the motor mechanism because it introduces a lag time during which force can be generated. It is possible that Pi release from the GDP·Pi-bound dimer is the dominant contributor to the lag time because it is known that the G interface can be strongly stabilized by the transition-state analog GDP·AlF$_4^-$ (23). Pi is produced while buried within the G interface and, therefore, slow release of Pi is to be expected. Modulation of the Pi release by the conformational state of the MM can also provide a mechanism for the strain control. Further work is needed to elucidate the role played by Pi in constriction. In addition, our computational model can be further validated and, possibly, refined by sophisticated force measurements of the MM using optical tweezers, further high-speed atomic force microscopy imaging of dynamin-mediated membrane remodeling (40, 43), or detailed
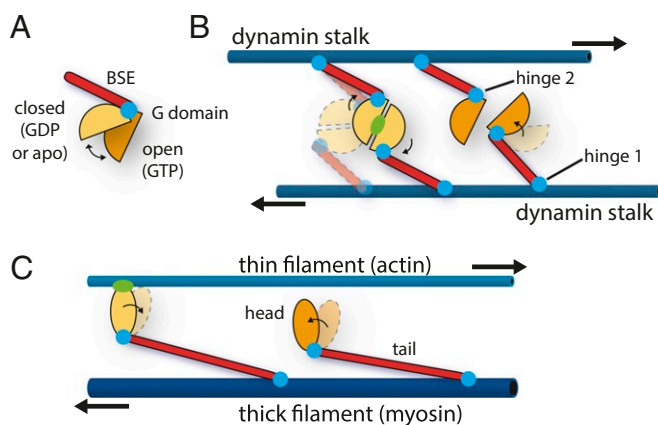
Fig. 7. A sliding-filaments cross-bridge mechanism for dynamin is suggested by our results. (*A*) smFRET indicates that the motor module exhibits strong nucleotide-dependent conformational shifts in solution. The transitions to closed and open represent, respectively, the power and the recovery strokes in the MM. (*B* and *C*) Comparison of operation schemes in dynamin and muscle myosin.

Ganichkin et al.
Quantification and demonstration of the collective constriction-by-ratchet mechanism in the dynamin molecular motor

kinetics experiments with dynamin mutants in combination with deformable membrane templates (53).

In summary, through integrating smFRET measurements, structural modeling, and filament simulations, we have shown that the conformational shifts in the dynamin motor module are strong enough to generate the necessary force to constrict biomembrane tubes when summed over several cooperating cross-bridges. In so doing, we have quantitatively validated the constriction-by-ratchet hypothesis and developed a model that can be generally applied to other membrane-remodeling motors, e.g., those involved in the maintenance and scission of mitochondria.

Materials and Methods

Cloning, Expression, and Purification. The pET-M11 vector was used to express a codon-optimized His6-tagged GTPase-BSE (MM) construct (Eurofins; residues 6 to 322 fused to residues 712 to 746 with a GSGSGS linker) in BL21 (DE3) Rosetta 2. Cells were grown at 37 °C to an OD600 of 0.4 and the protein was expressed in the presence of 0.15 mM Isopropyl β-d-1-thiogalactopyranoside (IPTG) overnight at 25 °C in terrific broth (TB) medium, supplemented with 34 μg/mL of chloramphenicol and 50 μg/mL of kanamycin. Cells were harvested by centrifugation, resuspended in buffer A (20 mM HEPES (4-(2-hydroxyethyl)-1-piperazineethanesulfonic acid)-NaOH, pH 7.5, 500 mM NaCl, 15 mM imidazole, 5% glycerol) and lysed in a microfluidizer. The cleared lysate after centrifugation was incubated for 30 min with 5 mL Ni-NTA resin at 4 °C on a rocking platform. Afterward, Ni-NTA beads were washed in batch three times with buffer A and transferred into a gravity-flow 20-mL column. Column material was further washed with 10 column volumes (CV) of buffer A supplemented with 2 mM ATP and 5 mM $MgCl_2$ and then with 2 CV of buffer A containing 50 mM imidazole. Eventually, the protein was eluted with 5 CV of buffer A containing 250 mM imidazole. The His6 tag was cleaved by incubation with Tobacco Etch Virus nuclear-inclusion-a endopeptidase during overnight dialysis against buffer A without imidazole. Subsequently, the protein was reapplied to the Ni-NTA column, collected in the flow-through fraction, and further purified via size-exclusion chromatography (SEC) on an S200 26/600 Superdex column with running buffer C (20 mM HEPES-NaOH, pH 7.5, 150 mM NaCl). Fractions containing the pure protein were pooled, concentrated to 30 to 50 mg/mL, aliquoted, and shock frozen in liquid nitrogen. The MM wild-type construct as well as various mutant variants were purified following the same protocol. For protein labeling with Alexa fluorophores or for experiments exploring metal-mediated dimerization of the MM constructs, the following mutations were introduced individually or in combination: T165C, R318C, N112C, K142H, N183H. Point mutations in the MM construct were introduced using QuikChange site-directed mutagenesis (Agilent). Cysteine mutations were used for covalent attachment of Alexa Fluor dyes and their locations were chosen to avoid any obvious functional disruption. See *SI Appendix* for methods specific to the crystallization and characterization of the Zn^{2+}-stabilized dimer.

Protein Labeling with Fluorescent Probes. Thiol-reactive fluorescent dyes (ThermoFisher Scientific) were used for site-specific labeling of cysteines in MM variants. Using Alexa Fluor 488 as donor and Alexa Fluor 594 as acceptor provides a Föster distance of 5.4 nm (54, 55). The T165C variant was used to determine the dissociation constants of the artificial dimer and the R318C/N112C double mutant for smFRET measurement. To reduce cysteines, 250 μL of a protein solution at 30 to 40 mg/mL was incubated with 20 mM dithiothreitol (DTT) for 1 h on ice, following DTT removal by gel filtration on an S200 10/300 column equilibrated with buffer F (20 mM HEPES-NaOH, pH 7.5, 5 mM $MgCl_2$, 150 mM NaCl, 10 mM KCl). The concentrated proteins were mixed with the corresponding thiol-reactive dye in a 1:2 M ratio (protein:dye) and incubated for 1 h at room temperature (RT). In the case of double labeling by Alexa Fluor 488 and 594, the reaction was started with addition of Alexa Fluor 488 to the protein solution in a 1:0.66 (protein:dye) molar ratio. After 40 min of incubation at RT, Alexa Fluor 594 dye was added in a 1:2 (protein:dye) molar ratio and the reaction was continued for 1 h at RT. The labeling process was terminated by the addition of 10 mM DTT. After 5 min incubation at RT, insoluble material was removed by centrifugation and the sample was applied to a second round of SEC to remove unreacted dye and DTT. Labeling efficacy was calculated according to the manual of Thermo Fisher Scientific; a typical range was 90 to 100%. All fluorescence-based functional and GTP hydrolysis assays for the monomeric form of the MM constructs were performed in buffer 1 (20 mM HEPES-NaOH, pH 7.5, 150 mM KCl, 4 mM $MgCl_2$). Experiments with the artificially dimerized form of the MM-HH variant were performed in buffer 2 (20 mM HEPES-NaOH, pH 7.5, 150 mM KCl, 4 mM $MgCl_2$, 160 μM $ZnSO_4$). All experiments were carried out at RT if not otherwise stated.

Single-Molecule FRET. Single-molecule FRET experiments were performed with a MicroTime 200 confocal system (PicoQuant) equipped with an Olympus IX73 inverted microscope and two pulsed excitation sources (40 MHz) controlled by a PDL 828-L "Sepia II" (PicoQuant). Pulsed interleaved excitation (PIE) (56) was used to identify molecules with active acceptor and donor dyes. Two light sources, a 485-nm diode laser (LDH-D-C-485; PicoQuant) and a white-light laser (Solea; PicoQuant) set to an excitation wavelength of 585 nm, were used to excite the donor and the acceptor dyes alternatingly. The laser intensities were adjusted to 100 μW at 485 nm and 30 μW at 585 nm (Pm100D; Thor Laboratories). The excitation beam was guided through a major dichroic mirror (ZT 470-491/594 rpc; Chroma) to a 60×, 1.2-NA water objective (Olympus) that focuses the beam into the sample. The sample was placed in a homemade cuvette with a volume of 50 μL (quartz 25-mm diameter round coverslips [Esco Optics], borosilicate glass 6-mm diameter cloning cylinder [Hilgenberg], Norland 61 optical adhesive [Thorlabs]). All measurements were performed at a laser power of 100 μW (485 nm) and 30 μW (585 nm) measured at the back aperture of the objective. Photons emitted from the sample were collected by the same objective and after passing the major dichroic mirror (ZT 470-491/594 rpc; Chroma), the residual excitation light was filtered by a long-pass filter (BLP01-488R; Semrock) and sent through a 100-μm pinhole. The sample fluorescence was detected with two channels. Donor fluorescence and acceptor fluorescence were separated via a dichroic mirror (T585 LPXR; Chroma) and each color was focused onto a single-photon avalanche diode (SPAD) (Excelitas) with additional bandpass filters: FF03-525/50 (Semrock) for the donor SPAD and FF02-650/100 (Semrock) for the acceptor SPAD. The arrival time of every detected photon was recorded with a HydraHarp 400M time correlated single-photon counting module (PicoQuant) and stored with a resolution of 16 ps.

Photons from individual molecules, separated by less than 100 μs, were combined into bursts if the total number of photons exceeded 30. Photon counts were corrected for background, acceptor direct excitation, and different detection efficiencies of the individual detectors. A PIE stoichiometry ratio $S < 0.7$ was used to identify molecules with an active acceptor. Identified bursts were corrected for background, differences in quantum yields of donor and acceptor, different collection efficiencies in the detection channels, cross-talk, and direct acceptor excitation. FRET histograms were fitted with a combination of Gaussian functions.

The labeled MM construct was diluted to a concentration of approximately 50 pM in 20 mM HEPES-NaOH, pH 7.5, 150 mM KCl, 4 mM $MgCl_2$ in the absence or presence of increasing amounts of GTP, GTPγS, GMP-PCP, and GDP. To prevent surface adhesion of the protein and to maximize photon emission, 0.001% Tween 20 (Pierce) was included in the buffer. All measurements were performed at 23 °C.

In the presence of saturating concentrations of GTP and GTP analogs (>1 mM; *SI Appendix*, Fig. S4C), a significant closed population remained, which could not be fully explained by unbound MM (predicted to <2% based on the determined affinities) or GDP contamination. The purity of GTP was 99.4% and that of GTPγS was 95%, as determined by high-performance liquid chromatography (HPLC).

Stopped-Flow Kinetic Measurements. All fast kinetic measurements were carried out on a Chirascan stopped-flow accessory unit equipped with an independent light-emitting diode power source (Applied Photophysics). For nucleotide-binding studies, fluorescent mant-substituted nucleotides were used. The dye fluorescence was excited at 350 nm and the fluorescence change monitored through a Schott 395-nm cutoff filter. To measure k_{on} values, increasing concentrations of MM construct (2, 3, 4.5, 7, 10.5, 15, and 20 μM) were titrated to 1 μM mant-nucleotide. For each concentration, at least five traces originated from the same sample were averaged. A linear regression was performed and the slope provided k_{on} with error given by the standard deviation in the slope. For quenching experiments to measure k_{rmoff}, 20 μM protein and 1 μM mant-nucleotide were mixed with 500 μM GTPγS or GDP. Three independent experiments were performed. Rates were determined by single exponential fits and the presented rate represents the average over the three experiments and the error the standard deviation. Error in K_d is determined by propagating the errors in k_{on} and k_{off}.

To detect conformational changes in the MM construct, FRET between Alexa Fluor 488 and 596 fluorescent pairs was recorded. Signals from both dyes were simultaneously detected using two photomultiplier tubes and a

8 of 11 | PNAS
https://doi.org/10.1073/pnas.2101144118

Ganichkin et al.
Quantification and demonstration of the collective constriction-by-ratchet mechanism in the dynamin molecular motor

Chroma ET525/50m bandpass and Schott 645-nm cutoff filter. G-domain/BSE opening was performed by mixing 5 μM of protein and 500 μM of GTPγS. Experiments for measuring G-domain/BSE closure were performed as follows: A total of 5 μM protein and 100 μM GTPγS were mixed with 2 mM GDP, where GDP will outcompete GTPγS for binding to the protein. Concentrations of reactants in both syringes of all stopped-flow experiments were two times higher compared to the measurement cell since they were diluted upon mixing in 1:1 ratio. Throughout this paper, indicated concentrations are those after mixing.

GTPase Assay. GTPase assays were performed in 20 mM HEPES-NaOH, pH 7.5, 150 mM KCl, 4 mM MgCl₂ containing 5 μM of the MM construct, and 1 mM GTP. The reaction was carried out at 37 °C. Upon starting the reaction, 2-μL reaction aliquots were withdrawn at different time points and mixed with 2 μL of 1 M HCl to stop the reaction and then diluted with 26 μL of HPLC buffer (100 mM potassium phosphate buffer, pH 6.5, 10 mM tetrabutylammonium bromide, 7.5% acetonitrile). Reaction products were quantified on an HPLC system from Agilent equipped with a Hypersil ODS-2 C18 column (250 × 4 mm). Each time-point measurement (five time points) was done in triplicate with the same sample. The specific hydrolysis rate for each protein concentration was computed by linear regression with error given by the standard deviation of the linear fit. To investigate the effect of Zn^{2+} on artificial dimer activity, 2.5, 10, 40, 80, 160, and 400 μM ZnSO₄ were added to the standard reaction. For testing concentration-dependent GTPase activity, reactions were performed in standard buffer at RT with 5, 15, 30, and 50 μM enzyme. The competition GTPase assay was performed by adding 0.21 or 0.85 mM of GDP to the reaction. See *SI Appendix, section S1.A.2* for details of the kinetic modeling of the competition assay.

MD Simulations. The conformational dynamics of the MM were studied by simplified structure-based models (SBMs) (57, 58), a method commonly employed to investigate protein dynamics. The dual-basin SBM was constructed in such a way that both the known open and closed MM structures were explicit energetic minima of it. The open structure was defined by chain A of the GMPPCP-bound MM (S_O) (6) and the closed structure by chain A of the GDP-bound MM (S_C) (24). The G domains between the two structures are nearly identical. The structural differences mainly reside in the positioning of the first BSE helix relative to the G domain (*SI Appendix, Fig. S5*). The weighting λ between open and closed in the simulation was determined by matching the simulated open/closed distributions to the smFRET data. See *SI Appendix* for details of the energy potential. Simulations were performed using GROMACS 4.5.3 (59) containing code edits implementing Gaussian contact interactions (available at). Single-basin simulation topologies were generated using the SMOG2 software (https://smog-server.org) (31, 60) with the forcefield "SBM_calpha + gaussian" (61) and combined using an in-house script. The temperature (T = 0.92 in reduced units) was chosen such that the average C_α atom rmsd in the closed MM agreed between a 100-ns explicit solvent simulation using AMBER99SB-ILDN at 310 K and the SBM. The temperature was maintained with stochastic dynamics with coupling constant 0.1 and the time step was 0.0005.

To model more closely the distance measured by smFRET, explicit dyes were attached at T165C and R318C. The dye consisted of a linear chain of six C_α beads connected by bonds 3.8 Å in length (as in Fig. 2C). The FRET efficiency for each snapshot was calculated based on $E = (1 + (d/d_0)^6)^{-1}$ using the distance d between the two terminal dye beads and $d_0 = 5.4$ nm. To compute the estimated FRET expected in either the open or the closed ensemble including thermal fluctuations (Fig. 2C) a λ of 0.5 (always open) and 1.2 (strongly closed) was used. For GTP bound or GDP bound a λ of 0.98 and 1.1 matched the smFRET histograms for GTP bound or GDP bound, respectively (*SI Appendix, Fig. S5D*). Note that the photon counting statistics in the experimental FRET system are sensitive to the timescale of moving between the open and closed states. If the conformational motion time is comparable to the time a single molecule dwells in the laser point (∼1 ms), the FRET distribution will become unimodal. Since separated peaks were observed in the experimental data, the dynamics observed must have been slower than 1 ms. Nonetheless, since averaging always tends to compress the peaks, the simulation data, which were not averaged, were expected to have wider separation between the peaks.

We note that the experimental smFRET histogram for GTP-bound MM appears to possess an intermediate state (Fig. 2A), although a two-state fit with skewed Gaussians is reasonable too. We have not included this intermediate state into the model because there is no crystal structure of it. For our purposes here, such an intermediate within GTP-bound dimers would have little effect, serving only to further flatten the already flat ℓ distribution.

The flexibility of hinge 1 (*SI Appendix, Fig. S6*) was estimated by a C_α SBM simulation equivalent to that just described except single basin, meaning that any term in the energy function containing the open structure was removed and $\lambda = 1$. A full monomer (chain A) taken from the apo (closed) crystal structure (20) was used to build the SBM. The PH domain along with stalk domain residues farther than 2 nm from hinge 1 were frozen during the simulation, mimicking its filament-bound state. The temperature was the same as above (T = 0.92) and the simulation was run for 10^8 time steps. For analysis of the structural fluctuations in terms of the helical coordinates, the frozen part of the stalk was fitted to a stalk domain in the helical reconstruction of Fig. 4A. Hinge 1 was identified by Proline 322 and hinge 2 was identified by Proline 27.

Mean Stall Forces. The probability distribution for the end-to-end lengths ℓ of cross-bridges is determined by the equilibrium distance distribution in prehydrolysis GTP-bound dimers, $P(\ell) = P_{GTP}(\ell)$. On the other hand, the contraction force is $F(\ell) = -dG_{GDP}(\ell)/d\ell = k_BT(d \ln P_{GDP}(\ell)/d\ell)$, where $G_{GDP}(\ell)$ is the Helmholtz free energy of a posthydrolysis GDP-bound MM dimer. The distance distributions for GTP- and GDP-bound MM dimers are presented in Fig. 4C. Thus, the mean force acting along the filament under the stall condition can be determined as

$$\langle F_s \rangle = \omega \int_{\ell_{min}}^{\ell_{max}} P(\ell)F(\ell) \sin \theta(\ell) d\ell, \quad \text{[1]}$$

where θ is the slant angle and ω is the probability (often referred to as the duty ratio) (32) to find a MM in the dimerized state. Refer to Fig. 4A for the definition of the geometry. The transverse component $\langle F_t \rangle$ is given by the same equation with $\sin \theta$ replaced by $- \cos \theta$.

The integral in Eq. 1 was computed by using the distribution $P(\ell) = A \exp[-G_{GTP}(\ell)/k_BT]$ and the force $F(\ell) = -dG_{GDP}/d\ell$ with the free energies G_{GTP} and G_{GDP} obtained in MD simulations, where A is a normalization constant for the probability distribution $P(\ell)$. In Eq. 1, we have $\sin \theta = \Delta s/\ell$ with $\Delta s = \sqrt{\ell^2 - h^2}$. Because of the ratchet property of hinge 1, only configurations with positive displacements Δs should be included when estimating the force. The minimal possible length of a link is $\ell_{min} = h$. Functions $P(\ell)$ and $F(\ell)$ were discretized in 0.5-nm steps and it was assumed that the filament radius is the same in the two rungs.

Elastic Treatment of the Filament and Membrane Tube. The code used to implement the constriction model (written in Java) is publicly available at https://bitbucket.org/jknoel/constrictionsimulation. A detailed formulation and analysis of the model for a dynamin filament on a membrane tube, in absence of the motor activity, was given in a previous publication (16). See *SI Appendix* for a full description. The dynamin filament was represented as an elastic polymer with each bead corresponding to a dynamin dimer. The membrane tube description was based on an axially symmetric continuous Helfrich elastic membrane with stiffness χ and under tension γ. The membrane stiffness $\chi = 24$ k_BT and the tension $\gamma = 0.03$ k_BT/nm^2 were chosen. At such a stiffness, the elastic energy cost of constricting the filament/membrane system is dominated by the membrane energy (*SI Appendix, Fig. S7E*). It should be noted that membrane composition and protein insertion can affect the resulting stiffness (62). As a point of reference a pure 1-palmitoyl-2-oleoyl-sn-glycero-3-phosphocholine (POPC) membrane has a stiffness around 30 k_BT. While the true stiffness at the scission neck remains unknown, the known active remodeling of the membrane composition and protein insertions should presumably act to facilitate the scission by shifting the membrane stiffness as low as possible.

Dynamin Motors in the Constriction Model. In the current study, the effects of motor GTPase activity were additionally incorporated into the above-described model. This entailed including explicit cross-bridges representing MM dimers and resolving the kinetics of GTPase cycles. Again, each simulation bead corresponds to a stalk dimer and, thus, has two MMs associated with it. A MM undergoes stochastic transitions between the five ligand states of the GTPase cycle, i.e., Apo and with the nucleotides GDP, GTP, GTP-D, or GDP-D (Fig. 3). The transitions between three monomeric states are characterized by the nucleotide on/off rates displayed in Fig. 1D. The bulk concentrations of GTP and GDP are chosen as 300 μM and 30 μM, respectively (these are typical physiological concentrations) (27). The Apo and GDP states cannot form cross-dimers. Binding of GTP by a MM alters the conformational state from the predominantly closed to the predominantly open at the rate of approximately 300 s^{-1} (Fig. 2 D and E). Since opening transitions are thus relatively fast, they are not explicitly resolved in the model. Instead,

Ganichkin et al.
Quantification and demonstration of the collective constriction-by-ratchet mechanism in the dynamin molecular motor

PNAS | 9 of 11
https://doi.org/10.1073/pnas.2101144118

all MMs in the GTP state are assumed to immediately go to the equilibrium open/closed distribution.

Two MM monomers in the GTP state can form the dimeric GTP-D state that represents a weak prehydrolysis dimeric state. The GTP state of a monomer transits to a GTP-D state at rate $k_{on}^{D}[MM]_{eff}$, provided that a valid MM partner for dimerization exists. A partner MM is valid if it is also in the GTP state and if the generated cross-dimer would satisfy the conditions $\ell < \ell_{max}$ and $\Delta s > 0$, with the latter condition taking into account the ratchet asymmetry of hinge 1. $\ell_{max} = 15$ nm is the natural extension limit of the dimer as can be seen in the GTP-bound free energy $G_{GTP}(\ell)$ (Fig. 4C). The geometry is explained in *SI Appendix*, Fig. S7A. Additionally, due to the excluded volume of the MM dimer, a valid cross-dimer cannot intersect any existing cross-dimers. The broad free energy basin for GTP-bound dimers, found in MD simulations, implies high flexibility (Fig. 4C). Therefore, no forces are generated by a GTP-D dimer in the model. The GTP-D dimer dissociates into two GTP MMs at rate k_{off}^{D}.

The transition from a prehydrolysis GTP-D dimer to the posthydrolysis GDP-D dimer takes place at rate k_{hyd}. Note that hydrolysis is chosen to occur simultaneously in both monomers; i.e., high cooperativity is assumed. Such cooperativity is suggested by our kinetic measurements showing that the hydrolysis is equally fast for the dimers containing either two GTP molecules or one GTP and one GDP (*SI Appendix*, section S1.A.2). The GDP-D dimer generates a force $\vec{F}(\ell)$ with the magnitude

$$F = \begin{cases} \frac{dG_{GDP}(\ell)}{d\ell}, & \ell < \ell_{max} \\ \frac{dG_{GDP}(\ell)}{d\ell}\big|_{\ell=\ell_{max}} + \eta(\ell - \ell_{max}), & \text{else} \end{cases} \quad [2]$$

and directed along the vector connecting the two MM attachment points (*SI Appendix*, Fig. S7A). The Helmholtz free energy $G_{GDP}(\ell)$ for the GDP-bound dimer is shown in Fig. 4C. As stated above, $\ell_{max} = 15$ nm. The parameter η is set to 3 $k_{B}T/nm^{3}$, so that the force steeply increases when ℓ exceeds ℓ_{max}.

The transition from a GTP-D state to the GDP-D state is irreversible due to hydrolysis. The GDP-D state can be left through dissociation into two MM monomers, each in the GDP state, at rate k_{diss}. When the strain dependence of this rate was taken into account, this was done by choosing

$$k_{diss}(\Delta s) = \begin{cases} k_{diss}, & \Delta s > 0 \\ \infty, & \text{else.} \end{cases} \quad [3]$$

Thus, an oppositely strained dimer dissociates immediately. In the model without strain dependence, k_{diss} remains constant regardless of the displacement Δs.

In kinetic simulations involving transitions between the states, the Gillespie algorithm is often used (63). In the present study, explicit stochastic simulations of the GTPase cycle were, however, carried out, because most of the computer time was already needed for integrating the equations of motion for the membrane and the beads. The weighting times of transitions obeyed an exponential distribution with a single rate parameter; i.e., the probability of a transition with rate k within time Δt is $1 - \exp(-k\Delta t) \approx k\Delta t$ for $k\Delta t \ll 1$. The transition times (inverse of transition rates) between states were all much longer than the integration time step δt of 10 ns. Therefore, the probability of a transition occurring during a single time step was taken to be $k\delta t$. The small time step was dictated by the membrane description that had to capture the lipid flows. As a characteristic example, a 1-s simulation (i.e., 10^{8} time steps) for a 200-bead filament on a 600-nm-long membrane tube required 5 h on a single core of the Intel Xeon E5-2695 v3 2.30-GHz central processing unit.

The nucleotide association/dissociation rates are given in Fig. 1D. Some GTPase-cycle parameters could not be directly measured (Fig. 3). Unless otherwise noted, $k_{on}^{D}[MM]^{eff} = 3 \times 10^{5}$ s^{-1}, $k_{hyd} = 175$ s^{-1}, and $k_{off}^{D} = 10^{5}$. The duty ratio ω was varied between 0.37 and 0.94 by changing k_{diss} between 100 s^{-1} and 3.3 s^{-1}. See *SI Appendix*, section S1.B for further discussion of the choice of the GTPase-cycle kinetic parameters.

Data Availability. All study data are included in this article and/or *SI Appendix*.

1. S. M. Ferguson, P. De Camilli, Dynamin, a membrane-remodelling GTPase. *Nat. Rev. Mol. Cell Biol.* **13**, 75–88 (2012).
2. S. Morlot, A. Roux, Mechanics of dynamin-mediated membrane fission. *Annu. Rev. Biophys.* **42**, 629–649 (2013).
3. O. Daumke, A. Roux, V. Haucke, BAR domain scaffolds in dynamin-mediated membrane fission. *Cell* **156**, 882–892 (2014).
4. R. Ramachandran, S. L. Schmid, The dynamin superfamily. *Curr. Biol.* **28**, R411–R416 (2018).
5. K. Faelber et al., Oligomerization of dynamin superfamily proteins in health and disease. *Prog. Mol. Biol. Trans. Sci.* **117**, 411–443 (2013).
6. J. S. Chappie et al., A pseudoatomic model of the dynamin polymer identifies a hydrolysis-dependent powerstroke. *Cell* **147**, 209–222 (2011).
7. L. Kong et al., Cryo-EM of the dynamin polymer assembled on lipid membrane. *Nature* **560**, 258–262 (2018).
8. A. Roux, K. Uyhazi, A. Frost, P. De Camilli, GTP-dependent twisting of dynamin implicates constriction and tension in membrane fission. *Nature* **441**, 528–531 (2006).
9. S. Morlot, M. Lenz, J. Prost, J.-F. Joanny, A. Roux, Deformation of dynamin helices damped by membrane friction. *Biophys. J.* **99**, 3580–3588 (2010).
10. S. Morlot et al., Membrane shape at the edge of the dynamin helix sets location and duration of the fission reaction. *Cell* **151**, 619–629 (2012).
11. S. Sever, H. Damke, S. L. Schmid, Garrotes, springs, ratchets, and whips: Putting dynamin models to the test. *Traffic* **1**, 385–392 (2000).
12. B. Antonny et al., Membrane fission by dynamin: What we know and what we need to know. *EMBO J.* **35**, 2270–2284 (2016).
13. M. Kaksonen, A. Roux, Mechanisms of clathrin-mediated endocytosis. *Nat. Rev. Mol. Cell Biol.* **19**, 313–326 (2018).
14. M. M. Kozlov, Fission of biological membranes: Interplay between dynamin and lipids. *Traffic* **2**, 51–65 (2001).
15. Z. A. McDargh, P. Vázquez-Montejo, J. Guven, M. Deserno, Constriction by dynamin: Elasticity versus adhesion. *Biophys. J.* **111**, 2470–2480 (2016).
16. J. K. Noel, F. Noé, O. Daumke, A. S. Mikhailov, Polymer-like model to study the dynamics of dynamin filaments on deformable membrane tubes. *Biophys. J.* **117**, 1870–1891 (2019).
17. Y. Kozlovsky, M. M. Kozlov, Membrane fission: Model for intermediate structures. *Biophys. J.* **85**, 85–96 (2003).
18. M. Pannuzzo, Z. A. McDargh, M. Deserno, The role of scaffold reshaping and disassembly in dynamin driven membrane fission. *eLife* **7**, 2270 (2018).
19. M. Lenz, J. Prost, J.-F. Joanny, Mechanochemical action of the dynamin protein. *Phys. Rev. E* **78**, 011911 (2008).
20. K. Faelber et al., Crystal structure of nucleotide-free dynamin. *Nature* **477**, 556–560 (2011).
21. M. G. J. Ford, S. Jenni, J. Nunnari, The crystal structure of dynamin. *Nature* **477**, 561–566 (2011).
22. J. S. Chappie et al., An intramolecular signaling element that modulates dynamin function in vitro and in vivo. *Mol. Biol. Cell* **20**, 3561–3571 (2009).
23. J. S. Chappie, S. Acharya, M. Leonard, S. L. Schmid, F. Dyda, G domain dimerization controls dynamin's assembly-stimulated GTPase activity. *Nature* **465**, 435–440 (2010).
24. R. Anand, S. Eschenburg, T. F. Reubold, Crystal structure of the GTPase domain and the bundle signalling element of dynamin in the GDP state. *Biochem. Biophys. Res. Commun.* **469**, 76–80 (2016).
25. M. L. Rennie, S. A. McKelvie, E. M. M. Bulloch, R. L. Kingston, Transient dimerization of human MxA promotes GTP hydrolysis, resulting in a mechanical power stroke. *Structure* **22**, 1433–1445 (2014).
26. Y. Chen et al., Conformational dynamics of dynamin-like MxA revealed by single-molecule FRET. *Nat. Commun.* **8**, 15744 (2017).
27. T. W. Traut, Physiological concentrations of purines and pyrimidines. *Mol. Cell. Biochem.* **140**, 1–22 (1994).
28. D. D. Binns et al., Correlation between self-association modes and GTPase activation of dynamin. *J. Protein Chem.* **18**, 277–290 (1999).
29. D. D. Binns et al., The mechanism of GTP hydrolysis by dynamin II: A transient kinetic study. *Biochemistry* **39**, 7188–7196 (2000).
30. Y.-J. Chen, P. Zhang, E. H. Egelman, J. E. Hinshaw, The stalk region of dynamin drives the constriction of dynamin tubes. *Nat. Struct. Mol. Biol.* **11**, 574–575 (2004).
31. J. K. Noel et al., Smog 2: A versatile software package for generating structure-based models. *PLoS Comput. Biol.* **12**, e1004794 (2016).
32. H. L. Sweeney, A. Houdusse, Structural and functional insights into the Myosin motor mechanism. *Annu. Rev. Biophys.* **39**, 539–557 (2010).
33. E. Cocucci, R. Gaudin, T. Kirchhausen, Dynamin recruitment and membrane scission at the neck of a clathrin-coated pit. *Mol. Biol. Cell* **25**, 3595–3609 (2014).

10 of 11 | PNAS
https://doi.org/10.1073/pnas.2101144118

Ganichkin et al.
Quantification and demonstration of the collective constriction-by-ratchet mechanism in the dynamin molecular motor

34. A. Grassart *et al.*, Actin and dynamin2 dynamics and interplay during clathrin-mediated endocytosis. *J. Cell Biol.* **205**, 721–735 (2014).

35. C. Veigel, S. Schmitz, F. Wang, J. R. Sellers, Load-dependent kinetics of myosin-V can explain its high processivity. *Nat. Cell Biol.* **7**, 861–869 (2005).

36. Y. Oguchi *et al.*, Load-dependent ADP binding to myosins V and VI: Implications for subunit coordination and function. *Proc. Natl. Acad. Sci. U.S.A.* **105**, 7714–7719 (2008).

37. M. Iwaki, A. H. Iwane, T. Shimokawa, R. Cooke, T. Yanagida, Brownian search-and-catch mechanism for myosin-VI steps. *Nat. Chem. Biol.* **5**, 403–405 (2009).

38. M. Kaya, Y. Tani, T. Washio, T. Hisada, H. Higuchi, Coordinated force generation of skeletal myosins in myofilaments through motor coupling. *Nat. Commun.* **8**, 16036–16013 (2017).

39. S. Watanabe, E. Boucrot, Fast and ultrafast endocytosis. *Curr. Opin. Cell Biol.* **47**, 64–71 (2017).

40. T. Takeda *et al.*, Dynamic clustering of dynamin-amphiphysin helices regulates membrane constriction and fission coupled with GTP hydrolysis. *eLife* **7**, e30246 (2018).

41. R. A. Obar, C. A. Collins, J. A. Hammarback, H. S. Shpetner, R. B. Vallee, Molecular cloning of the microtubule-associated mechanochemical enzyme dynamin reveals homology with a new family of GTP-binding proteins. *Nature* **347**, 256–261 (1990).

42. H. Damke, T. Baba, D. E. Warnock, S. L. Schmid, Induction of mutant dynamin specifically blocks endocytic coated vesicle formation. *J. Cell Biol.* **127**, 915–934 (1994).

43. A. Colom, L. Redondo-Morata, N. Chiaruttini, A. Roux, S. Simon, Dynamic remodeling of the dynamin helix during membrane constriction. *Proc. Natl. Acad. Sci. U.S.A.* **114**, 5449–5454 (2017).

44. S. Gao *et al.*, Structure of myxovirus resistance protein a reveals intra- and intermolecular domain interactions required for the antiviral function. *Immunity* **35**, 514–525 (2011).

45. T. F. Reubold *et al.*, Crystal structure of the dynamin tetramer. *Nature* **525**, 404–408 (2015).

46. C. Fröhlich *et al.*, Structural insights into oligomerization and mitochondrial remodelling of dynamin 1-like protein. *EMBO J.* **32**, 1280–1292 (2013).

47. A. Kadosh, A. Colom, Y. Ben, A. Roux, T. Shemesh, The tilted helix model of dynamin oligomers. *Proc. Natl. Acad. Sci. U.S.A.* **116**, 12845–12850 (2019).

48. M.-J. Huang, R. Kapral, A. S. Mikhailov, H.-Y. Chen, Coarse-grain model for lipid bilayer self-assembly and dynamics: Multiparticle collision description of the solvent. *J. Chem. Phys.* **137**, 055101 (2012).

49. R. Vasan, S. Rudraraju, M. Akamatsu, K. Garikipati, P. Rangamani, A mechanical model reveals that non-axisymmetric buckling lowers the energy barrier associated with membrane neck constriction. *Soft Matter* **16**, 784–797 (2019).

50. A. V. Shnyrova *et al.*, Geometric catalysis of membrane fission driven by flexible dynamin rings. *Science* **339**, 1433–1436 (2013).

51. J.-P. Mattila *et al.*, A hemi-fission intermediate links two mechanistically distinct stages of membrane fission. *Nature* **524**, 109–113 (2015).

52. H. E. Huxley, The mechanism of muscular contraction. *Science* **164**, 1356–1365 (1969).

53. T. J. Pucadyil, S. L. Schmid, Supported bilayers with excess membrane reservoir: A template for reconstituting membrane budding and fission. *Biophys. J.* **99**, 517–525 (2010).

54. B. Schuler, E. A. Lipman, W. A. Eaton, Probing the free-energy surface for protein folding with single-molecule fluorescence spectroscopy. *Nature* **419**, 743–747 (2002).

55. B. Schuler, H. Hofmann, Single-molecule spectroscopy of protein folding dynamics–expanding scope and timescales. *Curr. Opin. Struct. Biol.* **23**, 36–47 (2013).

56. B. K. Müller, E. Zaychikov, C. Bräuchle, D. C. Lamb, Pulsed interleaved excitation. *Biophys. J.* **89**, 3508–3522 (2005).

57. B. Jana, J. N. Onuchic, Strain mediated adaptation is key for myosin mechanochemistry: Discovering general rules for motor activity. *PLoS Comput. Biol.* **12**, e1005035 (2016).

58. J. K. Noel, J. N. Onuchic, "The many faces of structure-based potentials: From protein folding landscapes to structural characterization of complex biomolecules" in *Computational Modeling of Biological Systems*, N. Dokholyan, Ed. (Springer, Boston, MA, 2012).

59. S. Pronk *et al.*, GROMACS 4.5: A high-throughput and highly parallel open source molecular simulation toolkit. *Bioinformatics* **29**, 845–854 (2013).

60. J. K. Noel, P. C. Whitford, J. N. Onuchic, The shadow map: A general contact definition for capturing the dynamics of biomolecular folding and function. *J. Phys. Chem. B* **116**, 8692–8702 (2012).

61. H. Lammert, A. Schug, J. N. Onuchic, Robustness and generalization of structure-based models for protein folding and function. *Proteins Struct. Funct. Bioinf.* **77**, 881–891 (2009).

62. R. Dimova, Recent developments in the field of bending rigidity measurements on membranes. *Adv. Colloid. Interface Sci.* **208**, 225–234 (2014).

63. S. Kubo, T. Niina, S. Takada, Molecular dynamics simulation of proton-transfer coupled rotations in ATP synthase FO motor. *Sci. Rep.* **10**, 8225 (2020).

Ganichkin et al.
Quantification and demonstration of the collective constriction-by-ratchet mechanism in the dynamin molecular motor

PNAS | 11 of 11
https://doi.org/10.1073/pnas.2101144118